1 # From space-time landslide susceptibility to landslide risk forecast

2 Tengfei Wang[1,2], Ashok Dahal[2], Zhice Fang[2,3], Cees van Westen[2], Kunlong Yin[1*], Luigi Lombardo[2]

3 [1] Faculty of Engineering, China University of Geosciences, Wuhan, 430074, China;

4 [2] Faculty of Geo-Information Science and Earth Observation (ITC), University of Twente, Enschede, AE 7500, Netherlands;

5 [3] Institute of Geophysics and Geomatics, China University of Geosciences, Wuhan, 430074, China;

6 * Corresponding author: Kunlong Yin (yinkl@cug.edu.cn)

7

8 **Abstract**: The literature on landslide susceptibility is rich with examples that span a large number of
9 topics. However, the component that pertains to the extension of the susceptibility framework toward
10 space-time modeling is largely unexplored. This statement is even more valid when looking at the
11 landslide risk context, where hardly any scientific contribution investigates risk dynamics in space and
12 time. This manuscript proposes a modeling protocol where a dynamic landslide susceptibility is obtained
13 via a binomial Generalized Additive Model whose inventories span nine years (from 2013 to 2021). To
14 perform the analyses, the data cube is organized with a mapping unit made of slope units (26,333)
15 repeated over an annual temporal unit (for a total of 236,997). This phase already features a number of
16 interesting modeling experiments that have hardly appeared in the landslide literature (e.g., variable
17 interaction plots). However, the main innovative effort is in the subsequent phase of the protocol we
18 propose, for we used climate projections of the main trigger (rainfall) to obtain future estimates of yearly
19 susceptibility patterns. These are also combined with the projection of urban settlements and associated
20 populations to obtain a dynamic risk model (under the assumption that vulnerability = 1). Overall, this is
21 a unique example of such a modeling routine and a potential standard to be followed for administrations
22 to make informed decisions on future urban development.

23

25 ## 1 Introduction

26 Historical advancements in landslide susceptibility modeling (through data-driven solutions)
27 explored a number of themes, spanning from the most suitable mapping unit on to base the analyses (e.g.,
28 Van Den Eeckhaut et al., 2009; Schlögel et al., 2018), to the most suitable predictor set (e.g., Budimir et al.,
29 2015; Ozturk et al., 2021), passing from experiments on the most appropriate sampling strategies
30 (Yilmaz, 2010; Conoscenti et al., 2016) to take and encompassing solutions to remove potential biases
31 due to incomplete inventories (Steger et al., 2016; Lima et al., 2021).

32 As for the most recent trends in landslide susceptibility modeling, most contributions focused on the

choice of modeling architectures able to ensure the highest predictive performance (Reichenbach et al., 2018; Lima et al., 2022). In this overall scenario, very isolated efforts have been put forward to move toward space-time solutions (Samia et al., 2017; Lombardo et al., 2020). These are models whose structure allows for modeling the distribution of landslide presence/absence instances simultaneously across the geographic space and across time. The way they usually work is to incorporate explanatory variables whose spatiotemporal variation reflects changes in the distribution of multi-temporal landslide occurrences. This can be done explicitly (e.g., using rainfall or vegetation parameters; Wang et al., 2022a; Mondini et al., 2023) or at the latent level (Lombardo et al., 2018, 2019). Some exceptions to this rule do exist and they represent very innovative examples where the typical structure of space-time data-driven solutions is used to mimic landslide early warning systems (e.g., Steger et al., 2022; Nocentini et al., 2023).

However, even if recent studies are pointing towards an increasing interest in dynamic landslide predictions, these are mostly confined to the occurrence probability case (Segoni et al., 2018; Lombardo and Tanyas, 2020). In other words, the number of contributions beyond the susceptibility context, even including space-time cases, is a minority (Tyagi et al., 2022). This is an issue that certainly exists for landslide hazard assessment contributions (see, Van Westen et al., 2006), and becomes even more evident in the case of landslide risk research (see, Corominas et al., 2014). Focusing on risk aspects, what stands out is that most of the contributions on landslide risk are site-specific (Dai et al., 2002; Glade et al., 2005) and mainly involve pure spatial assessments (Lateltin et al., 2005; Abella and Van Westen, 2007). Conversely, hardly any examples can be found where the landslide risk assumes space-time connotations (Remondo et al., 2008; Rossi et al., 2019).

The main reasons behind such discrepancies are the requirement of such type of assessment. For instance, risk assessment requires data on the distribution of exposure (Pellicani et al., 2014; Emberson et al., 2020) and vulnerability (Galli and Guzzetti, 2007; Kaynia et al., 2008). The former can still be found to some extent, with products that report building, infrastructure, and population density distributions. However, vulnerability information (Ahmed, 2021; Peduto et al., 2017) and specifically on vulnerability curves estimated for specific infrastructures (Quan Luna et al., 2011; Uzielli et al., 2015) are hardly available, especially when the scale of the analyses involves large spatiotemporal domains (Pascale et al., 2010; Luo et al., 2023). And yet, this constitutes the most relevant information for decision-makers because it is precisely the combination of exposure and vulnerability that controls the potential losses due to a given landslide occurrence (Petley, 2012; Papathoma-Köhle et al., 2015).

In this context, we devised our research question and the experimental design presented in this contribution. Specifically, due to the prohibitive task behind the acquisition of vulnerability data over

large regions and over time, we hypothesize that if a landslide occurs, it would damage irreparably any structure in its path. This is certainly a strong assumption but it would allow to produce landslide risk estimates if building and population data are combined with a susceptibility map. To this idea, we add a further dimension by framing the proposed routine in a space-time modeling context. We do so thanks to a rich landslide database collected over a decade in the northeastern sector of Chongqing, China. There, a systematic landslide mapping protocol has been set up over the years due to historical disastrous events (e.g., Zhao et al., 2018), equipping local authorities and academic institutions with complete multi-temporal inventories. Due to analogous reasons, the area is also equipped with a dense rain gauge network (Chen et al., 2019), making it an ideal case for testing space-time modeling techniques. There, we will calibrate and validate a space-time susceptibility model with the intent of using it as a base for future simulations, which we will then combine with urban and population projections to obtain future landslide risk scenarios.

2 Study area

2.1 Geography and geological condition

The study site is located in the southeast of Chongqing, China, and extends over an area of ~34,000 km^2 (see Fig. 1a). It is located on the northeastern edge of the Sichuan Basin, and as a result of an ongoing tectonic compression started in the late Mesozoic, the topography features numerous folds and high peaks, low hills, and incised valleys. The mountain ranges are oriented either NE–SW or E–W, with mountain elevations between 800-2700 m, while valleys occupy a much lower position in the topographic profile, with elevations ranging from 300-1000 m (see Fig. 1b). Due to the complex nature of the terrain, slopes cover a wide range of 0-60°, mostly centered at 25° (see Fig. 1c). The geomorphology is structurally controlled, featuring anticlinal mountains and synclinal valleys, with trends being roughly consistent with the directions of tectonic lineaments. The Yangtze River, the longest river in Asia, flows from west to east in the study area.

2.2 Rainfall condition

The region is exposed to a subtropical monsoon climate, with four distinct seasons and high precipitation discharges. Thousands of rain gauges have been installed in the last decade to monitor the rainy weather and characterize the monsoon-influenced humid subtropical climate. These are all new-generation weather stations, automatically recording and airing the digital transcripts to the data center daily. The very same data was shared from the meteorological agency of Chongqing to support this research, covering the period from January 1st 2013 to December 31st 2021, and corresponding to the

96   precipitation signal captured across 729 rain gauges (see Fig. 1d).
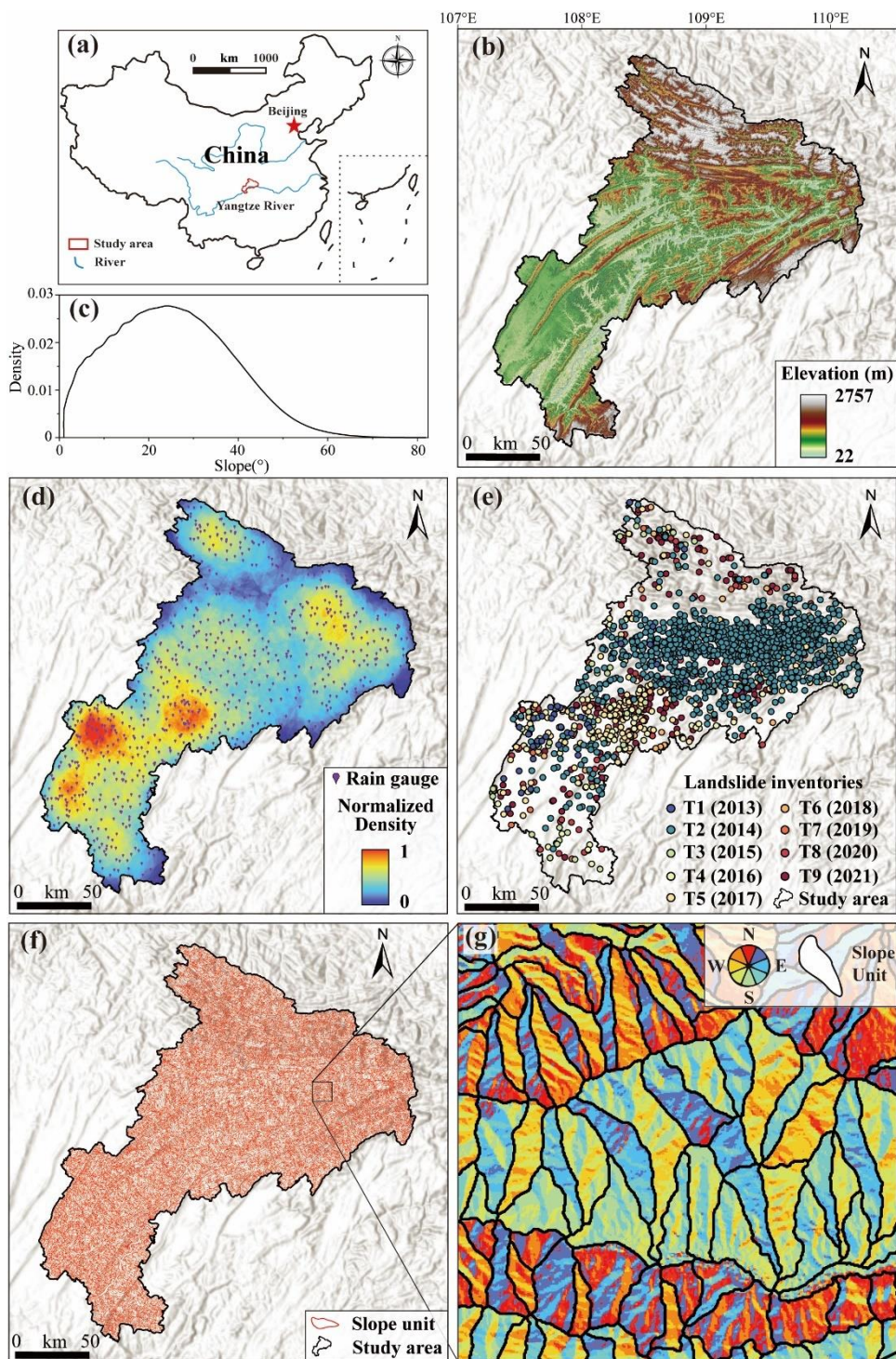
97

98   Figure 1: Panel (a) locates the study site concerning the Chinese territory; Panel (b) presents an overview of the

99   terrain; Panel (c) graphically shows the summary statistics of the slope steepness; Panel (d) geographically plots

100   the distribution density of the rain gauges; Panel (e) represents the multi-temporal landslide inventories; Panels

101   (f) and (g) show the slope unit partition and a dedicated zoom, respectively.

102   **2.3 Landslide inventory**

Chongqing widely hosts landslide-prone steep terrains, especially in the northeast sector, where landslides tend to concentrate along the Yangtze River and some of its tributaries, especially in the regions of Wanzhou, Yunyang, and Wushan. The genesis of the failure mechanism in the area has been documented in several scientific contributions, highlighting the primary role of seasonal, intense, and prolonged rainfall events (see, Zhang et al., 2023), followed by the fluctuation of reservoir water level and anthropic interventions involving slope cuts. From 2013 to 2021, the number of landslides with detailed records (location and date) in the study area reached a total number of 2978, out of which, 2142 landslides occurred just in 2014 (see Fig. 1e). These account for 72 % of the total failures over the 9 examined years, and were triggered by an extreme storm (Li et al., 2022). The vast majority of landslides manifest as shallow translational slides. As for the materials the failures mostly involve, these correspond to sandstone, mudstone, and intercalations of the latter into the first (Wang et al., 2019).

3 Material and methods

3.1 Mapping and temporal units

To predict the occurrence of landslides in an area, it is necessary to first select a suitable mapping unit. Among the units explored in previous studies, four main types can be found: geomorphological units (Meijerink, 1988; Seijmonsbergen et al., 2013), unique condition units (Calcaterra et al., 2010; Titti et al., 2021), slope units (Carrara et al., 1991), and grid-cells (Fang et al., 2020; Lima et al., 2021). Slope units have recently gained more and more attention, as they represent the morpho-dynamic response of slopes in which the landslides initiated. As a result, specifically for data-driven models, they offer a partition for which any landslide activation should be mostly independent (or very weakly dependent) from a potential failure occurring in an adjacent slope. For this reason, the "slope unit" (SU) is selected here to be the designated mapping unit in this study (Alvioli et al., 2016). In short, SU can be mapped between drainage and divide lines. Their calculation relies on the same foundation behind catchment delineation (Jenson and Domingue, 1988)because they theoretically correspond to half-basins (Carrara, 1988). Notably, the study area includes both rough terrain and near-flat areas in the form of plains, tablelands, and water bodies. The latter usually correspond to trivial areas where no landslide can physically take place. The latest version of the software *r.slopeunits* by (Alvioli et al., 2016) allows one to remove flat areas from the SU generation, excluding them based on the results pass by the *r.geomorphon* module (Jasiewicz and Stepinski, 2013). After a number of sensitivity (unreported) tests, the final number of SU was 26,333, ranging in size from $2.04 \cdot 10^4 \ m^2$ to $1.5 \cdot 10^7 \ m^2$ ($\mu = 1.25 \cdot 10^6 \ m^2$, $\sigma = 1.23 \cdot 10^6 \ m^2$). This corresponds to an average density of one SU approximately every 1.3 km^2 (see Fig. 1f and 1g).

134   As for how we partitioned the temporal dimension, we opted for a yearly unit (YU). Therefore, the
135   landslide inventory was divided into nine consecutive YUs. The combination of the spatial and temporal
136   dimensions eventually led to a total of 236,997 SUs (26,333 SUs multiplied by 9 YUs).

3.2 Covariates

137

138   The covariates set includes environmental characteristics related to geology, geomorphology, and
139   meteorology to cover different aspects related to the genesis of landslides. Some of them featured properties
140   that remain essentially constant within the time scale of the analyses. For instance, lithological classes can
141   be considered time-invariant. Analogously, terrain characteristics also exhibit a slow rate of temporal
142   variation and can also be approximated to be time-invariant (or at least there is no topographic data
143   acquired frequently enough to support a different solution). Conversely, vegetation density and rainfall
144   patterns do change at a fast rate, allowing for a space-time model to incorporate their dynamic signal.

145   Table 1 lists the initial covariate set we considered for this study. It includes 14 static covariates and
146   3 dynamic ones. Out of the static group, ten are derivatives of a 30 m·30 m resolution digital elevation
147   model (DEM). We recall here that a SU partitions the landscapes into high-order half-basins with an
148   average areal extent of $1.25 \cdot 10^6 m^2$. Therefore, their surface expression can host hundreds or even
149   thousands of 30 m·30 m grid cells. For this reason, we summarized the corresponding grid-based covariates'
150   distribution in a SU, through their respective mean and standard deviation values. We also computed a
151   static covariate capable of expressing the structural geology typical of each SU. We did this by
152   combining terrain characteristics with local measurements of strata direction and dip angles. To do so,
153   we followed the same approach shown by Luo et al. (2021). We then categorized the resulting map
154   categorized the results into 3 structural classes (dip slope, anti-dip slope, and cross-dip slope) and assigned
155   the predominant type to each SU. The predominant type criterion was also used to aggregate the soil type
156   (see, Li et al., 2009) and land use (see, Gong et al., 2020) 1:250,000 scale information per SU.

157   We also aggregated on a SU basis the yearly sum and daily maximum rainfall interpolated from the local
158   rain gauge network. To perform the interpolation, we opted for an Ordinary Kriging (Cressie, 1988). As
159   for the aggregation method, we assigned the mean rainfall value per SU.

160   The normalized difference vegetation index (NDVI) was also featured in the covariate set by computing
161   the mean value of all annual mean values across pixels falling in a given SU.

162

163

164

165

Table 1: Summary of initial covariates used in this study

Type	Covariates	Description	Source
Static	$Slope_\mu$	Terrain slope mean	30·30m DEM
	$Slope_\sigma$	Terrain slope St. dev.	
	$PLCR_\mu$	Planar curvature mean	
	$PLCR_\sigma$	Planar curvature St. dev.	
	$PRCR_\mu$	Profile curvature mean	
	$PRCR_\sigma$	Profile curvature St. dev.	
	$Northness_\mu$	Northness mean	
	$Northness_\sigma$	Northness St.dev.	
	$Eastness_\mu$	Eastness mean	
	$Eastness_\sigma$	Eastness St.dev.	
	$SLST$	Majority class of slope structure in each slope unit	Terrain Slope and tendency, Rock formations tendency, and dip
	$Lithology$ $Soil\ Type$ $Land\ use\ type$	Majority class in each slope unit	Lithological map, 1:250,000 Soil type map, 1:250,000 Land use type, 1:250,000
Dynamic	$Daily\ maximum$ $rainfall$	Maximum daily rainfall per year in each slope unit	National rain gauge
	$Annual\ sum$ $rainfall$	Sum rainfall per year in each slope unit	
	$NDVI\ \mu$	Mean NDVI value per year in each slope unit	Landsat 7 images from Google engine

3.3 Rainfall projections

As part of the modeling protocol, we present in this manuscript, we will train a space-time susceptibility model, from which we will simulate future landslide occurrence probabilities corresponding to various rainfall projections. Therefore, it was necessary to introduce a pre-processing step to obtain rainfall scenarios. The pre-processing method approach first calculates the annual average, maxima, and standard deviation from the projected climate change scenarios from Coupled Model Intercomparison Project CMIP-5 models (Taylor et al., 2012), which has been bias-corrected by using the method developed by Thrasher et al. (2012) and distributed under the NASA Earth Exchange Global Daily Downscaled Projections NEX-GDDP program of National Aeronautics and Space Administration (NASA). From these bias-corrected products, we selected the Representative Concentration Pathways (RCP) -4.5 scenario, which represents the climate projections showing the level of radiative forcing by greenhouse gas emissions stabilizing at 4.5 W/m^2 by 2100. This is because the projection of landslide hazard is estimated for the next eight years, and climate extremes due to much harsher scenarios (such as RCP-8.5) which are expected by the end of the century, are still not fully surfaced. With the selected scenario and different models, we ensembled the precipitation scenarios by averaging the annual maximum and mean projections obtained from different models. The standard deviation, however, is used as a quality check to ensure there are very unlikely precipitation scenarios that can unnecessarily elevate the

susceptibility. With the annual ensembled mean, we then computed the expected annual total precipitation by multiplying the ensembled mean by 365. This is because the daily climate projection products are not very reliable and full of uncertainties; therefore, their direct summation may increase bias. Nevertheless, their annual average forecast is much more reliable and likely to occur; thus, calculating total annual precipitation by multiplying the annual mean by 365 provided a rough estimate of precipitation with higher certainty than the summation of daily products. This approach is repeated from 2022-2030 for each year to calculate the rainfall projections for the next eight years.

3.4 Generalized additive model

Generalized Additive Models (GAMs) are a class of statistical models capable of estimating the functional relation existing between dependent and independent variables accommodating for both linear and nonlinear cases (Hastie and Tibshirani, 1987). In short, this allows for estimating single regression coefficients for covariates that are linearly linked to the response, and an array of regression coefficients for covariates that are modeled nonlinearly. The latter is mostly achieved by using splines, whose nature depends on the nonlinear dependence the user is interested to model(Hastie, 2017).

GAMs are suitable to model a number of statistical distributions, welcoming exponential families such as binomial, Poisson, Gamma, and more. In the context of landslide susceptibility studies, the response variable expresses two conditions, reflecting whether a given slope may be stable or unstable (Brenning, 2008). For this reason, we opted for a binomial GAM, whose generic structure can be denoted as follows:

$$\eta\left(\pi\right) = \log(\frac{\pi}{1-\pi}) = \beta_0 + \sum_{n=0}^{\text{\# lin. cov.}} \beta_n X_n + \sum_{i=0}^{\text{\# nonlin. cov.}} f_i x_i \tag{1}$$

where η is the logit function, π is the probability of at least a landslide to occur in a given Slope Unit, β_0 is the global intercept, β_n are the regression coefficients linearly estimated for each of the covariates X_n in the model, and f_i is spline regression functions estimated for each of the covariates x_i in the model.

Notably, a strict definition of a spatial statistical model requires it to treat different observations distributed across the geographic space. For instance, interpolators treat measurements as a function of reciprocal distances (Babak and Deutsch, 2009). But, in most landslide susceptibility examples this is usually not the case, as the probability assigned to any given mapping unit varies in space purely as a function of covariate values. In other words, mapping units that are located close to each other are usually treated in the same way as those that are located far away. Analogous considerations can be made in relation to the temporal dimension. A strict definition of a temporal statistical model requires it to treat different instances distributed across time. For instance, in time-series analysis, model estimates computed for a specific moment also depend on the signal recorded before, and the strength of such dependence usually decays with time (Beck

215 et al., 1998). In other words, temporal observations that are close in time are treated differently as compared

216 to observations that are recorded much earlier. We recall now that the stable/unstable labels in this work are

217 assigned to SU on an annual basis.

218   Therefore, in addition to terrain, geological and meteorological covariates, we also included a spatial and

219 a temporal effect to induce proximity dependence in the two respective dimensions. In turn, this defines our

220 model as a space-time Binomial GAM, which we implemented by using the "mgcv" package (Wood, S. and

221 Wood, M.S., 2015) in "R" (Ihaka and Gentleman, 1996).

222 **3.5 Model validation**

223   Our GAM model serves both explanatory and predictive purposes. The explanatory component

224 involves interpreting the functional relations estimated for each selected covariate from a geomorphological

225 perspective. For instance, if a model would return a negative influence of the slope steepness over the

226 susceptibility, this would not reflect the physical understanding of the failure mechanism. This is one of

227 the main strengths of statistical models because they can be assessed both on the basis of their scientific

228 reasonability as well as the performance they produce. Here, we achieve these two elements by fitting a

229 model that uses 100% of the available spatiotemporal information. As for the performance assessment, we

230 recall here that the input of a susceptibility model consists of a vector of stable/unstable labels,

231 conventionally represented by zeroes and ones. However, the output of the model is not discrete but

232 expressed instead as a continuous range of probabilities. Consequently, when evaluating the performance

233 of any binary classifier, the requirement is always to convert a posteriori probability spectrum into a

234 sequence of zeroes and ones. These can then be matched against the original presence/absence

235 observations, obtaining what is commonly referred to as a confusion matrix. This is made of four

236 elements namely, True positives (TP), True negatives (TN), False Positives (FP), and False Negatives

237 (FN). From these, a number of performance derivatives can be obtained, both cut-off dependent and cut-

238 off independent. In this work, we assessed the performance by measuring TP / (FN + TP) and TN (TN +

239 FP). These fall in the cutoff-dependent category because a different probability threshold from the one

240 we set here at the Youden Index (Fluss et al., 2005), would lead to different accuracy values. Another

241 performance parameter we consider is the error rate, which corresponds to the average of the

242 misclassified cases (both FP and FN), normalized with respect to the total samples.

243   To estimate cutoff-independent performance, we opted for the ROC curve. This is obtained by

244 repeatedly classifying the susceptibility at varying thresholds and plotting each pair of TPR and FPR. Its

245 integral or AUC is commonly used as a model diagnostic with values around 0.5 considered unsuitable,

246 values of 1.0 to be considered ideal, and the transition between the two expressing an increase in

247   classification performance (Hajian-Tilaki, 2013).

3.6 Stepwise GAM

249   Covariate selection ensures an optimal set of parameters to build a given data-driven model on.
250 Generally, several approaches can be taken to perform this task, including for instance, Ridge (McDonald,
251 G.C., 2009) and LASSO (Amato et al., 2019) regressions, or a number of stepwise procedures (Agostinelli,
252 C., 2002). In this study, we used a step-wise GAM approach to remove redundant and non-informative
253 covariates. We, therefore, fitted a number of 17 individual GAMs, starting from the use of a single
254 variable (see Table 1). From them, we selected the covariate that led to the minimum Akaike Information
255 Criterion (AIC; Sakamoto et al., 1986) value. The process was sequentially run adding one variable at a
256 time, solving for all combinations that would lead first to the couple of covariates with the least AIC,
257 then to the triplet with the least AIC, and so on. We implemented this procedure in such a way that would
258 highlight the best model, which corresponds to the situation after which the AIC has a negligible decrease
259 even after adding new covariates.

4 Results

4.1 Covariates selection and goodness-of-fit

262   We use a forward-stepwise procedure to choose the best covariate set. Among all the tests we have
263 run, we featured covariates used in the linear and nonlinear form and even included a few cases where we
264 allowed for variable interactions. In Figure 2a, we show an overview of some of these tests, already ranked
265 from the highest to the lowest AIC results, and concerning the last configuration we obtained (with linear and
266 nonlinear cases as well as interactions already pre-defined). We stress here that a stepwise selection requires
267 a factorial combination of all the considered variables even with a single covariate configuration. Therefore,
268 for conciseness and simplicity reasons, we report the essential information corresponding to the last test,
269 where the minimum Δ_{AIC} from one step to the next is reached at the inclusion of the $Slope_\sigma$, featuring each
270 covariate as a spline effect, except $Northness_\mu$ and $Slope_\sigma$ here used linearly. Notably, we also allowed for
271 variable interaction in the case of the *Daily maximum* and *Annual sum* of the rainfall, and for the *x* and *y*
272 locations of the slope units. The first interaction is chosen to reflect two aspects of the rainfall effect on the
273 yearly distribution of landslides, where the *Daily maximum* conveys the impulsive meteorological signal and
274 the *Annual sum* conveys the overall behavior. As for the combination of the *x* and *y* locations, this is meant
275 to ensure that proximal and far away slope units are treated differently, as prescribed for any spatial
276 model. We also point out the fact that the minimum Δ_{AIC} excludes the *Lithology* from the model, something

277 we interpreted because of its similarity to the *Soil type* and because the dominant landslide type in the multi-
278 temporal inventory corresponds to shallow failures. This particular covariate set then leads to a reference
279 space-time model whose goodness-of-fit is shown in Figure 2b with overall accuracies of positive and
280 negative cases of 82.12% and 75.13%, respectively. To these measures, the error rate of 0.248 and the
281 AUC of 0.87 attest for the excellent performance of the model (see, Hosmer and Lemeshow, 2000). However,
282 these goodness-of-fit considerations are mostly valid for the whole space-time classification process, and they
283 do not differentiate between the results obtained across each year constituting the whole domain. For this
284 reason, we opted to include Figure 2c. There, we showcased how the whole space-time domain can be
285 dissected on a yearly basis, providing an overview of year-specific susceptibilities against the original
286 presence/absence labels. In such a plot a suitable classifier would produce different probability densities for
287 slope units hosting landslides or not. Indeed, what we see is that across each year under consideration the
288 bulk of the two (presence/absence) probability distributions are quite far from each other. This in turn
289 indicates that our space-time model suitably discriminates stable and unstable slope units both in space
290 and time.
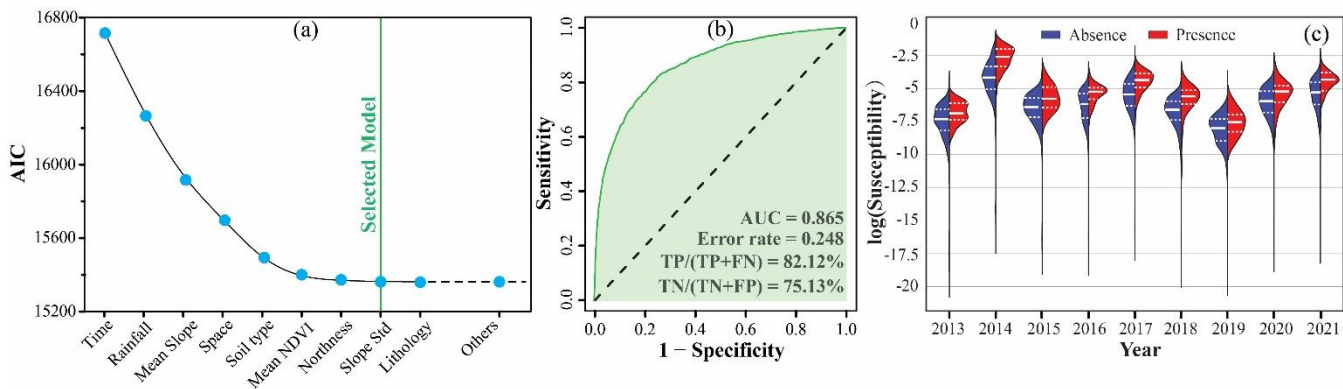
291

292 Figure 2: Panel (a) shows the results of the forward-stepwise covariate selection we implemented. Panel (b)
293 reports the corresponding goodness-of-fit measured in terms of the ROC curve and its AUC. Panel (c) fragments
294 on a yearly basis the overall performance overview already provided in panel b. This last panel offers a graphical
295 summary of the estimated susceptibility (shown in log scale for visualization purposes), plotted against the
296 original presence/absence data. White solid lines correspond to the mean value of the respective distributions,
297 whereas the width between the two white dotted lines corresponds to $\pm 1\sigma$.

298 **4.2 Covariate's effects**
299   Covariate effects are shown in Figures 3 and 4. The reason for this split is meant to highlight some
300 interesting aspects not usually explored in other landslide susceptibility contributions. In fact, Figure 3 offers
301 a unique view of the interaction effect between two rainfall parameters and how this combined effect
302 contributes to the probability of landslide occurrence in space and time. What we would like to highlight are

303   the two extremes of the regression coefficient range. The minimum regression coefficient is estimated for

304   large values of annual daily sum and relatively low maximum daily precipitation. As for the maximum

305   regression coefficients, these are obtained for large daily maximum values associated with relatively low

306   yearly cumulative precipitation. The way we interpret this signal is that large total rainfall data associated

307   with average daily maxima would correspond to meteorological conditions for which the landscape is

308   exposed to continuous "drizzle". Such prolonged, low-intensity rainfall may not have the capacity to

309   initiate shallow landslides, which we remind here constitutes the dominant landslide type in the study

310   area. As for the opposite situation, we interpret the large effect brought by large daily maxima associated

311   with relatively low total yearly precipitation as an indicator of impulsive cloudbursts capable of releasing

312   large quantities of rain (up to 300mm) in a relatively short amount of time. This situation may therefore modify

313   the slope equilibrium rapidly forcing a pore-pressure increase and consequently leading to a decrease in the
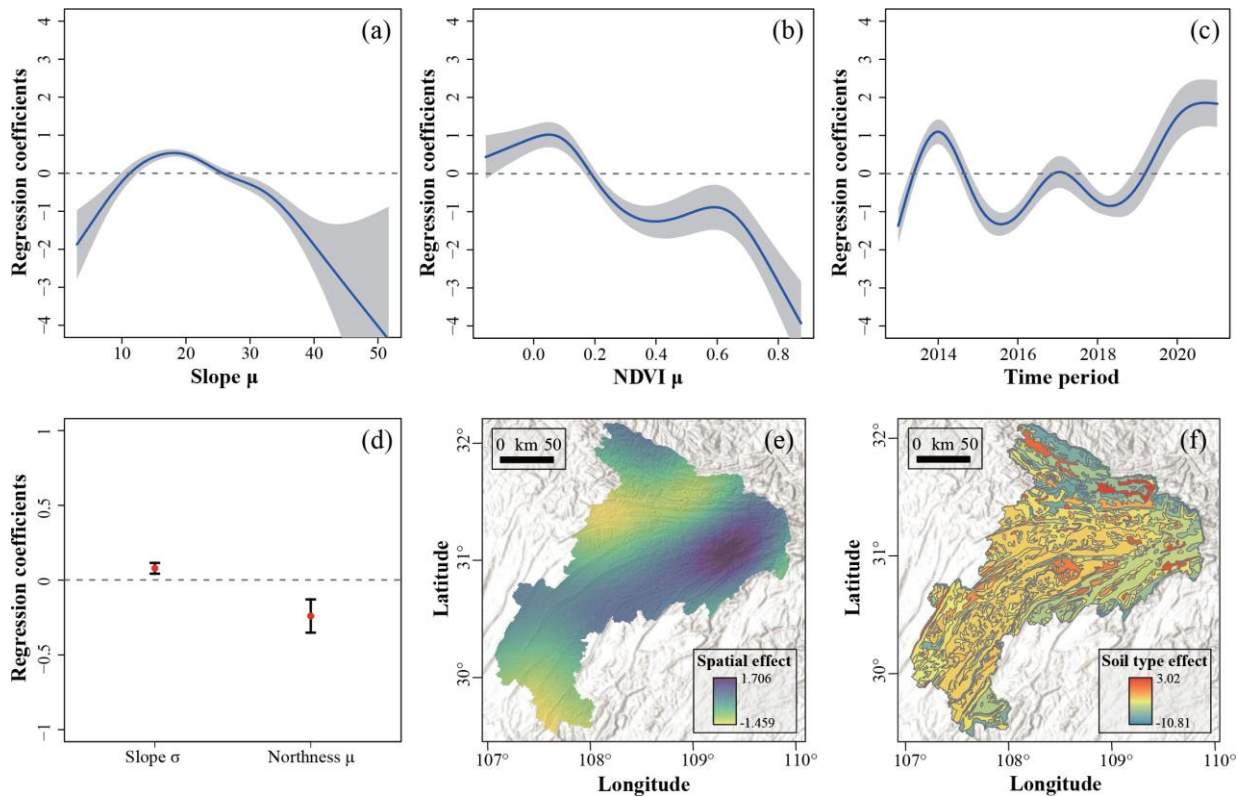
314   slope stability.
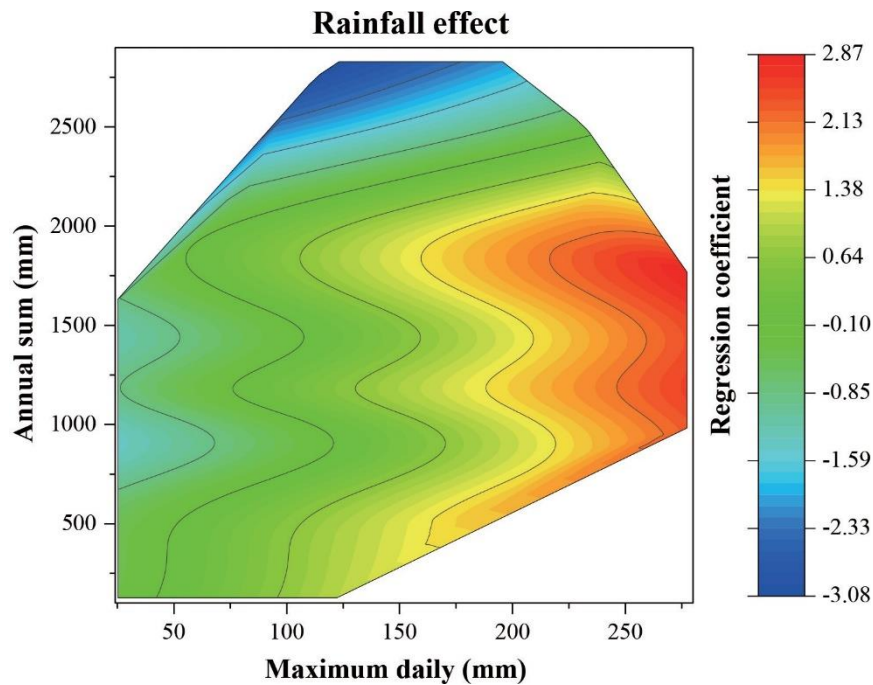
316   Figure 3: Summary of the variable interaction plot for the two rainfall indicators used in the model.

317   Moving onto a more common representation of covariate effects, in Figure 4a, we notice a spline effect in

318   the $Slope_\mu$ negatively contributes to the spatiotemporal probability of landslide occurrence in the range

319   between 0 and 12 as well as 28 to 53 average degrees per slope unit. Putting things into perspective, this is

320   a geomorphologically reasonable result as 0°-12° are slope characteristics typical of near flat to very gentle

321   slopes. As for the 28°-53° range, this may correspond to slope units too steep to host any potentially unstable

322   soil column.

In Figure 4b, the *NDVI* μ effects appear to follow an overall negative trend, where susceptible slopes are associated with bare conditions, at best covered by sparse vegetation ($-0.15 < NDVI\,\mu < 0.15$). Higher vegetation density indicators are all associated with negative regression coefficients. Such a pattern also appears to be geomorphologically sound, for dense vegetation may interfere with the splash effect of the rain as well as increase the soil stability through the root system. The last individual spline effect is depicted in Figure 4c, where the spikes in the regression coefficients are associated with years that have also recorded a high number of landslide occurrences. Two interesting observations need to be made here, the first one being the fact that the highest spike (2021) in the regression coefficient does not correspond to the year with the largest number of failures (2014). This may be because the rainfall signal is largely capable of explaining the landslides triggered in 2014, therefore limiting the temporal effect. As for the year 2021, the rainfall does not appear to be extreme, nor in its daily maximum expression nor its yearly sum. Therefore, the model may estimate a larger regression coefficient for this period, to be potentially attributed to unobserved or latent covariate effects (see Opitz et al., 2022, for further explanations).

Figure 4d reports the significant linear effects of *Slope$_\mu$* and *Northness$_\mu$*. The former is estimated with a positive contribution, something interpretable as a function of roughness. In fact, large variations of slope steepness within a single slope unit are indicative of rough conditions. This being said, it is also worth mentioning that the regression coefficient distribution, albeit significant, is not far away from the zero line, which implies a very limited effect overall. As for the second covariate, this marks a larger effect by comparison (the mean regression coefficient is farther away from the zero line). In turn, this implies that slopes that are facing south are the ones that are mostly associated with slope failures. Figures 4e and 4f respectively show the spatial and soil type effects. What stands out the most is that the spatial effect contributes by promoting unstable SUs to the very south, and in the northern sector where the pattern shows a NE-SW direction. Interestingly, this is also the main direction of the tectonic lineaments present in the area. Conversely, soil control on slope stability is much more spatially complex. For reasons of conciseness, we only report here the two major pedological classes contributing to the SU classification. Specifically, gravelly sands with a loamy component are associated with the largest regression coefficient ($\beta = 3.02$). Conversely, black soils negatively contribute to the space-time susceptibility ($\beta = -10.16$).

Figure 4: Marginal covariate plots: panels (a, b, c) show the effect of ordinal covariates (mean slope steepness, mean vegetation density, and time period) whose effect is passed to the model through a spline. Panel (d) highlights the linear effect of the standard deviation of the slope in a given slope unit together with the mean exposition to the north. Panel (e) translates the results of the spatial effect into map form. Similarly, the categorical contribution of the soil type is reported in panel (f) also in its geographic form.

4.3 Space-time predictive performance

Before presenting the results of our space-time random cross-validation (RCV), we would like to remind the readers of an important aspect often neglected in the literature. We initially recall that a validation procedure should highlight the model's capacity to suitably predict data that has not been featured as part of the calibration phase. However, this is not the only requirement of a robust performance assessment. Traditionally, one often assumes that the structure of the data may carry some degree of spatial autocorrelation and that in turn, this may optimistically bias the final performance. This is why Brenning (2012) prescribes spatial cross-validation routines, and Roberts et al. (2017) recommend space-time cross-validation routines, because, through these techniques, one can ensure any dependence structure in the data to be broken down, allowing for an unbiased predictive performance assessment. However, (Wadoux et al., 2021) recently challenged such statements, demonstrating that random cross-validation produces negligible differences as compared to spatial cross-validation routines. Considering these two radically opposite positions, in this work we opted for an RCV that we progressively pushed towards more

significant sample removals. In such a way, we would both equip our model with an RCV but also ensure that any spatiotemporal autocorrelation would be progressively weakened, allowing for a suitable assessment.

These results are shown in Figure 5, where each row represents a different percentage split in the RCV. Each column, represents a different aspect of the performance assessment, starting from reporting the cutoff independent assessment summarized via the ROC curves obtained for each of the 100 iterations. The subsequent two columns correspond to the accuracy (or confusion) plot for the positives and negatives, as well as the error rate box plots. Both metrics are obtained using a probability cutoff corresponding to the Youden index, reported in the fourth column. What stands out the most is that the performance is extremely stable. Irrespective of the portion of the data that we randomly extract for validation, the model performance essentially stays the same. The AUC values maintain an average very close to 0.84. The accuracy of the model in predicting absence cases essentially stays between 79% and 80%, whereas the same for the present instances is confined between 72% and 74%. This is also reflected in the error rate, being stable at around 0.21. These are important considerations that support our model not only as an explanatory tool but also as a robust predictive one.

384
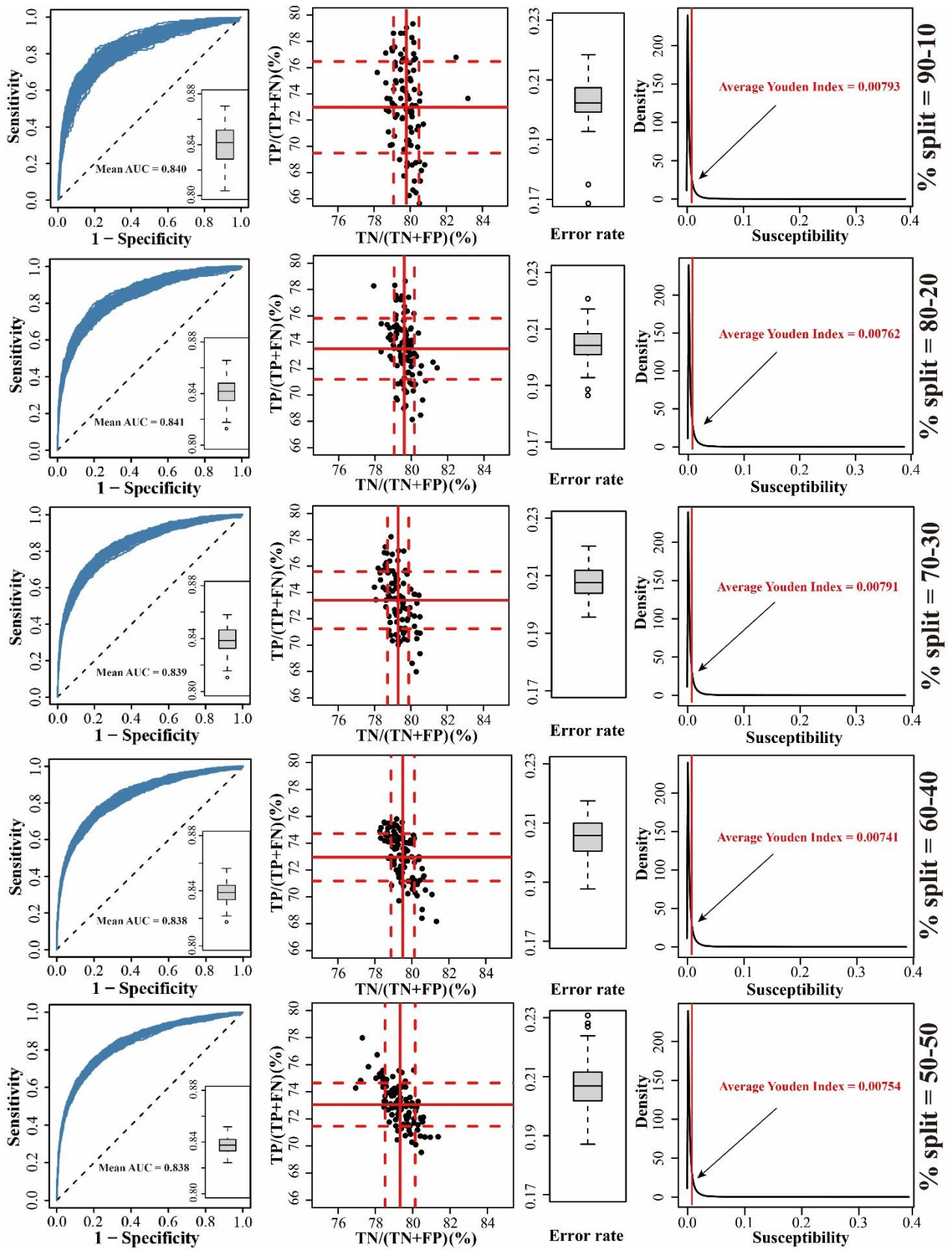
Figure 5: Random cross-validation performance summary of ROC, confusion, error ratio, and average Youden

index distribution in the 90/10, 80/20, 70/30, 60/40, and 50/50 selection ratios.

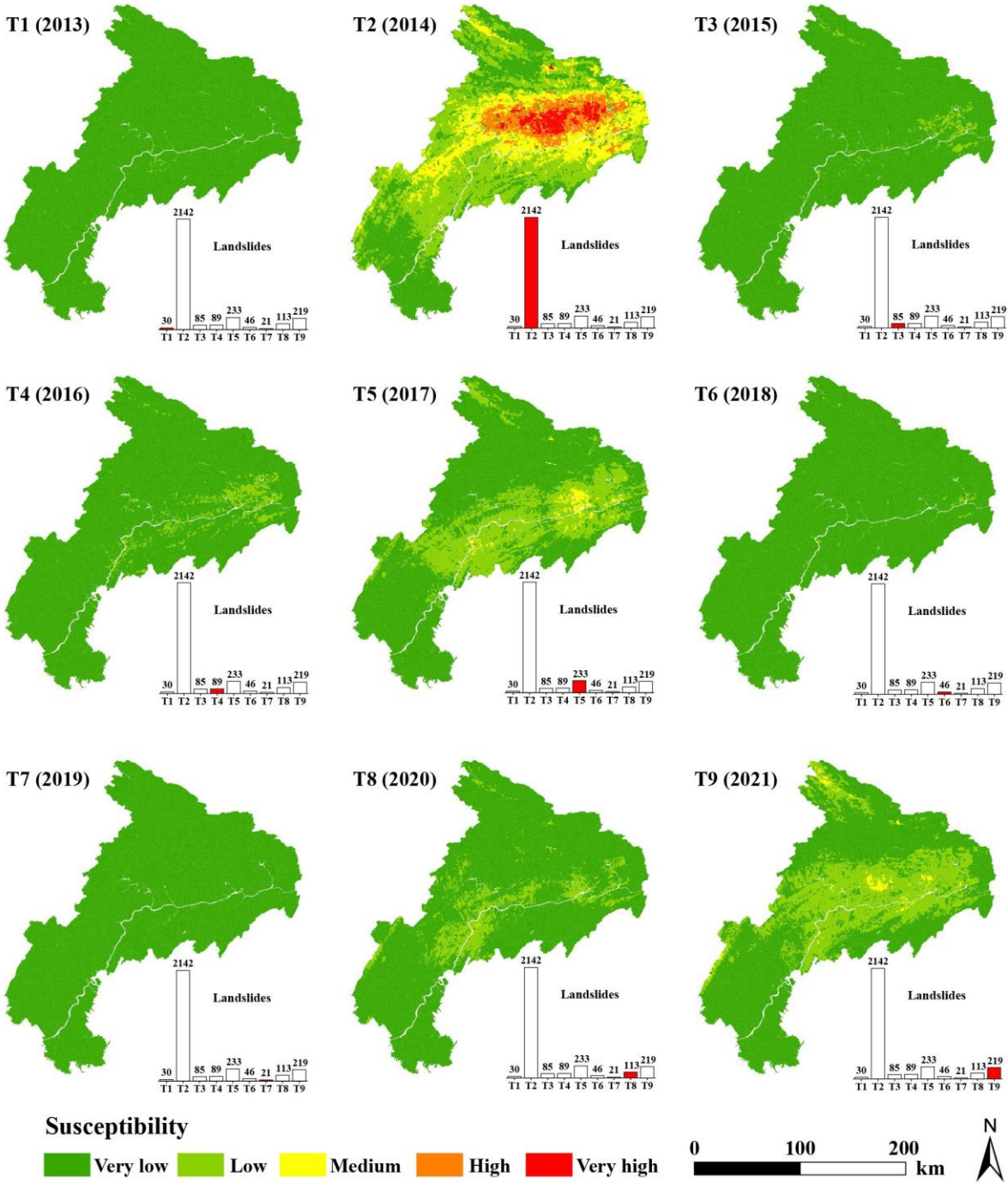387 **4.4 Susceptibility mapping**

388   Having demonstrated the predictive capacity of our space-time susceptibility model, in this section,

389 we translate the model results into maps. However, susceptibility maps need to undergo a further

390 processing step where the continuous spectrum of probability values is binned in a number of classes.

391 Therefore, finding suitable breaks corresponding to each class limit is required. Here we present this step in

392 Figure 6, where all the space-time probability domain is classified according to five classes following the

393 Jenks method (North, 2009). We recall here that this method starts from a pre-defined number of classes and

394 finds the cutoffs that minimize the intra-class variances.

395   The very same probability cutoffs have been used to plot the nine separate susceptibility maps shown in

396 Figure 7. There one can appreciate the flexibility of our space-time model in mimicking the overall yearly

397 landslide frequency (see nested bar plots) in the level associated with each susceptibility map.

398   This is particularly evident for the second map where 2142 out of 2978 occurred just in the year

399 2014. This level of consistency justifies the use of our space-time model for cartographic purposes

400 and the next section will be dedicated to the generation of future scenarios using a simulation approach.
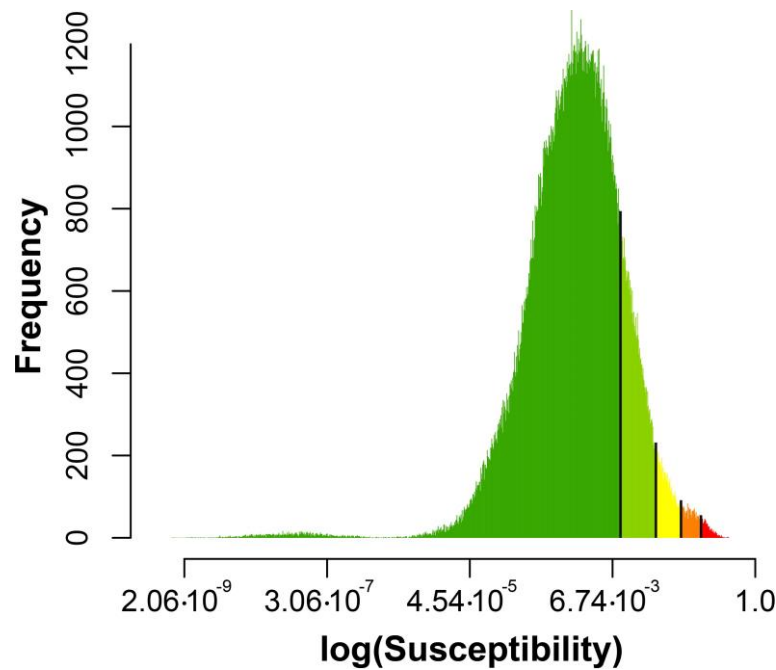
401

402 Figure 6: Jenks classification of the spatiotemporal distribution of fitted susceptibility values from 2013 to 2021.

403 We opted to plot the probability values in logarithmic scale because the original scale is very heavy-tailed, making

404 it difficult to graphically represent it.

Figure 7: Landslide susceptibility map for the year from 2013 to 2021. Continuous susceptibility values are grouped into five classes with Jenks classification.

4.5 Future risk forecasting

Generalizing data-driven susceptibility models is almost done exclusively in the spatial dimension, through a procedure commonly referred to as model transferability (Petschko et al., 2014; Wang et al., 2022b). Conversely, here we transfer our model in time using a plug-in simulation approach (see Lombardo and Tanyas, 2020). In other words: 1) we solve the predictive equation we obtained, 2) we keep all the

covariates as they are except the two rainfall parameters, 3) we remove the rainfall data estimated for the years 2013-2021, and 4) introduce the rainfall projected for the years 2022-2030. But, as interesting as such a procedure may be, it still does not convey any information on the expected risk local communities may be exposed to. For this reason, not only we simulated future landslide susceptibility scenarios, but we also collected two more exposure parameters in the form of future built-up areal extent (m^2) and the future number of inhabitants. A description of both parameters can be found in Lepetit et al. (2023) and they can be accessed at https://ghsl.jrc.ec.europa.eu/download.php?ds=pop.

The combination of estimated susceptibility, together with the two exposure parameters is shown in Figures 8 and 9. In the first case, one cannot assume the information to fully reflect the risk because it is not possible to assign a specific vulnerability curve to a generic layer reporting the expected built-up area distribution. However, if one would assume the vulnerability = 1, then the combination of the two layers would indeed depict the risk to the building and infrastructure. We recall here that the reference natural hazard corresponds to rapid landslides, and therefore, hypothesizing that a given built-up area would be hit by a fast-moving mass should not be an unreasonable assumption. Conversely, this issue does not affect the exposure data of the local population, which indeed would incur losses if they would find themselves in the path of a theoretical debris flow.

Going back to the individual figures' content, the two landslide risk maps highlight slightly different areas potentially requiring further attention. Built-up areas under the most threat from landslides are mostly located in the central sector of the northeast of Chongqing, irrespective of the year under consideration. As for the population, the same densely inhabited area appears to be likely exposed to landslide occurrences. However, right eastward of it, some interesting spatiotemporal patterns can be seen with the combination of highly likely landslide occurrence probabilities and expected inhabitants generating high-risk patches in the zoomed-in part of the maps.

We can also see that the worst-case risk scenarios determined by the susceptibility (lowest right panels in Figures 8 and 9) produce two slightly different patterns with the built-up area being more subjected to landslide risk as compared to the local expected population. One would expect the two exposure parameters to be mostly correlated. Therefore, such differences may be mostly interpreted with part of the built-up area being allocated to industrial activities and hence, to a lesser population density.

To confirm this interpretation, further analyzed the two exposure parameters and showed their spatiotemporal characteristics in Figure 10. There, one can notice that panel (a) projects an increase in expected built-up with time (from ~150 km^2 between 2022 and 2024 to ~200 km^2 between 2025 and 2029, and up to ~240 km^2). Conversely, the population is projected to slightly decay, starting from
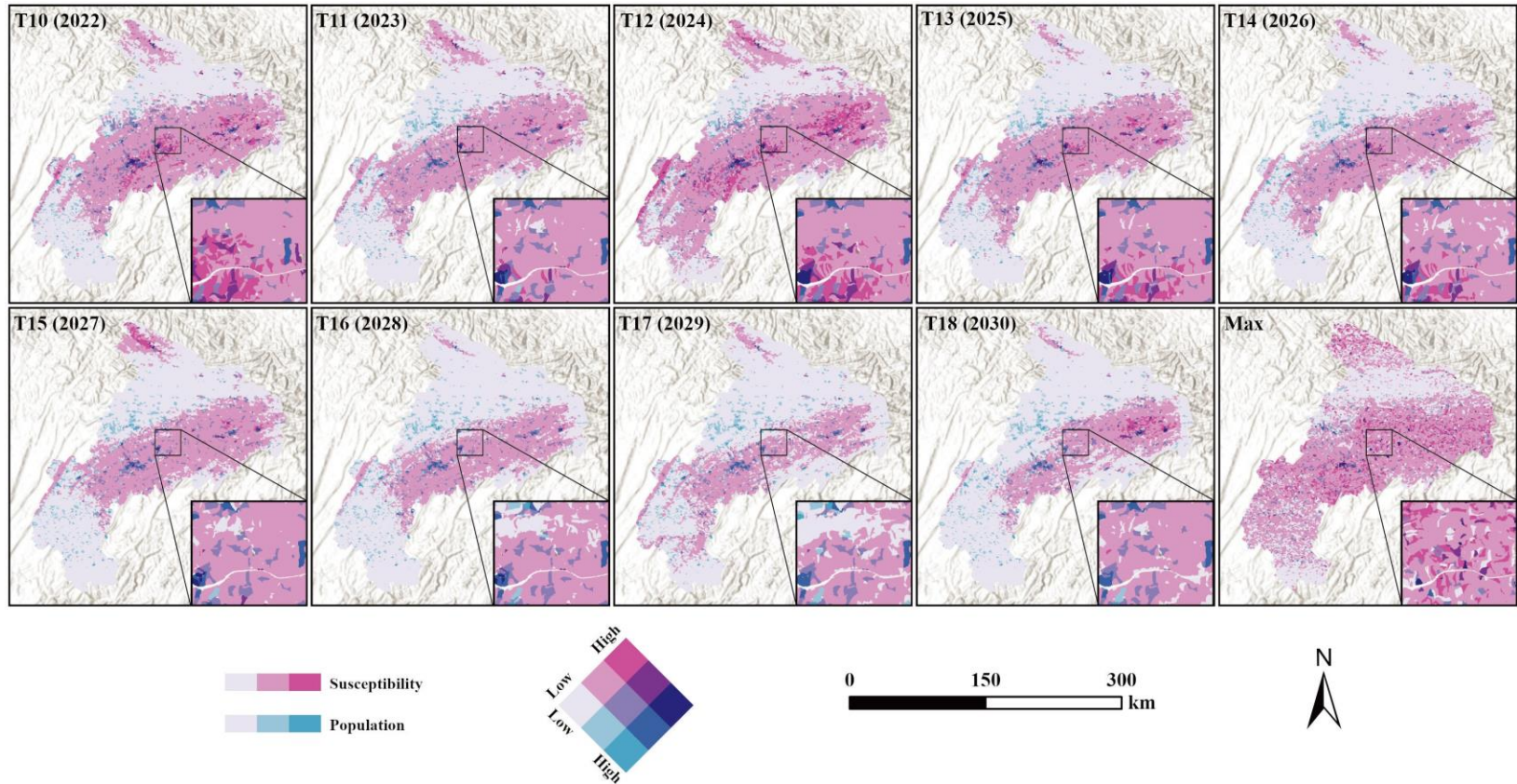
445

446

447

448
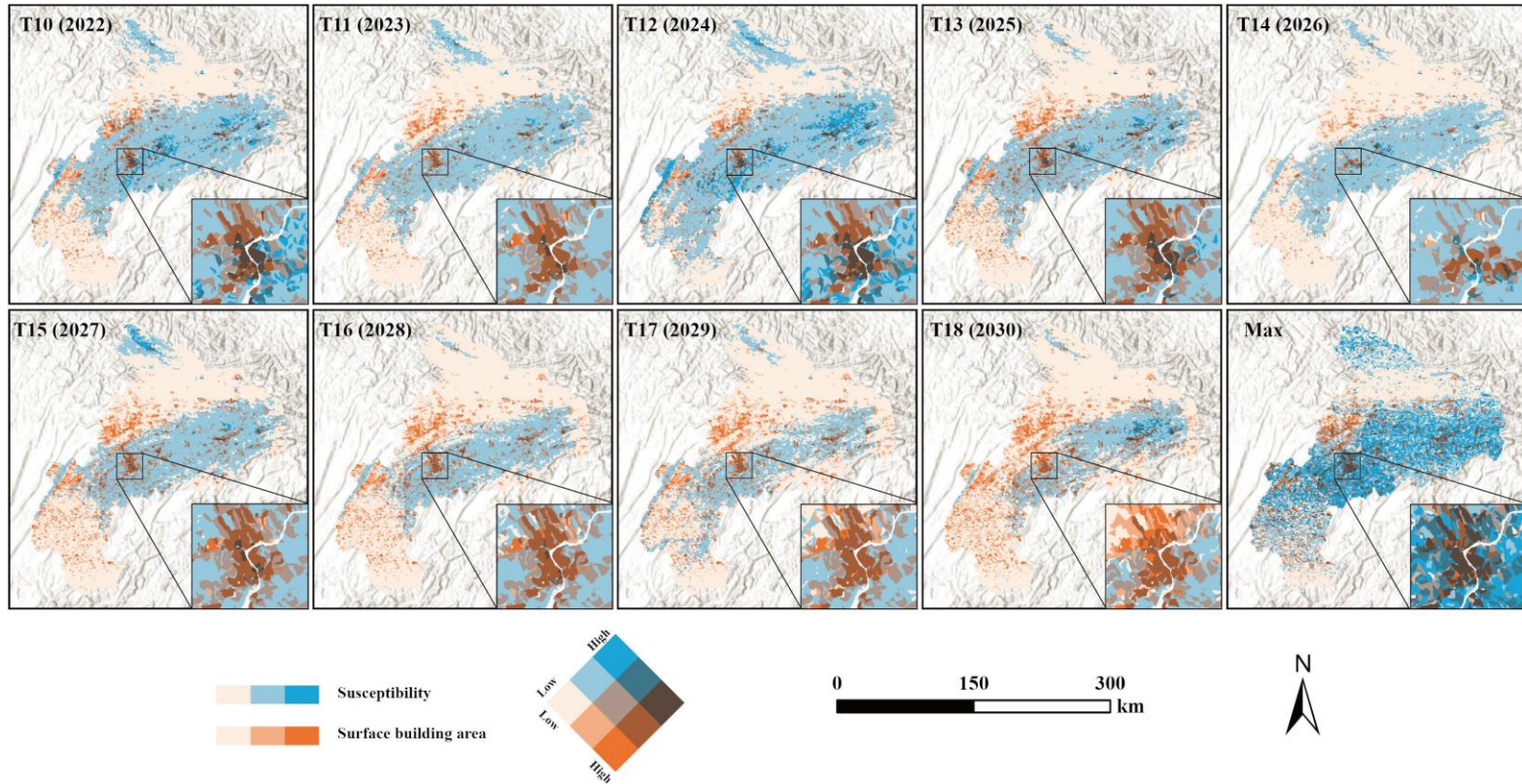
Figure 8: Impact-based scenarios obtained by combining landslide occurrence probability and built-up area projections. The first nine panels depict the yearly variation of landslide susceptibility, whereas the built-up area scenarios vary on a 5-yearly basis. The last panel corresponds to the worst combined scenario (max susceptibility and associated building distribution) out of the 9 projected years.

452

453

454

455

456

457

Figure 9: Impact-based scenarios obtained by combining landslide occurrence probability and the number of inhabitants projections. The first nine panels depict the yearly variation of landslide susceptibility, whereas the population scenarios vary on a 5-yearly basis. The last panel corresponds to the worst combined scenario (max susceptibility and associated population distribution) out of the 9 projected years.

around 8.2 million inhabitants in 2022 and reaching around 7.8 million in 2030. The same plots can be used to assess the goodness of local master plans. In fact, the proportion of built-up areas and populations in 2022 falls in both cases within a low susceptibility class much smaller as compared to the combination of medium and high classes. However, most of the built-up areas and inhabitants would be associated with the low susceptibility class in 2030.
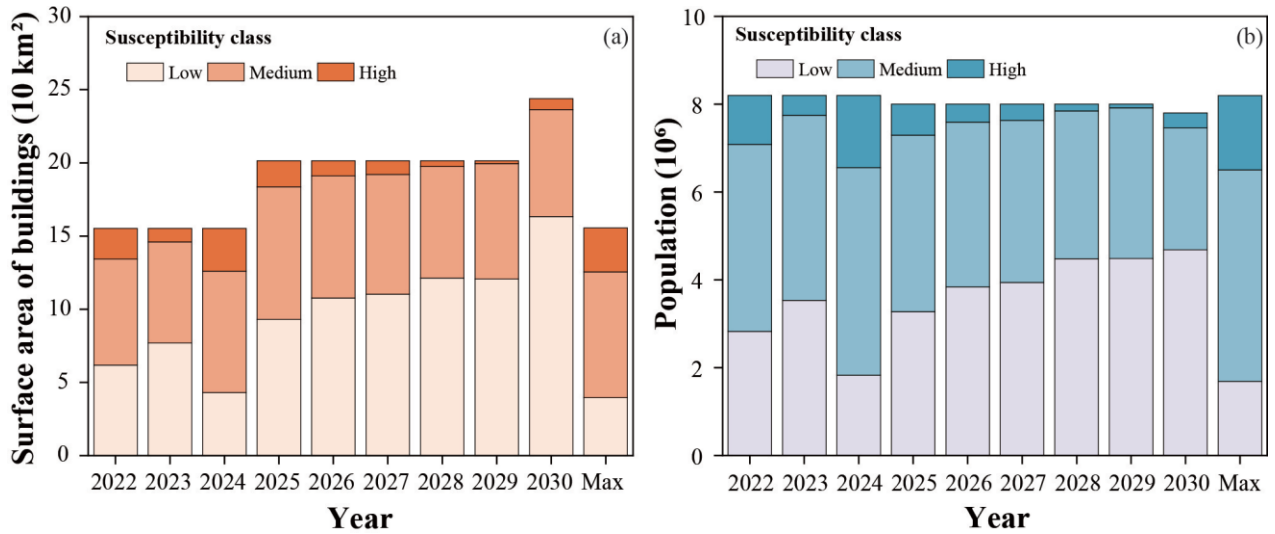
Figure 10: Distribution of projected built-up areas (a) and populations associated with specific susceptibility classes over the 9 projected years. The last stacked bar plot reports the two parameters for the respective cases where the space-time susceptibility has reached its maximum value per slope unit.

5 Discussion

This section is dedicated to scrutinizing our modeling protocol and its results, highlighting potential strengths and weaknesses. For this reason, below we dedicate two separate sections to the respective considerations.

5.1 Supporting arguments

Space-time susceptibility modeling is still largely unexplored (Reichenbach et al., 2018). Most of the current literature still uses landslide inventories where the temporal information is missing or left unused. For this reason, our modeling protocol already presents an example of state-of-the-art data-driven solutions for landslide spatiotemporal prediction. And even in the framework of an already limited literature, in this work, we further nested a number of sub-experiments that by themselves offer "food for thought" for landslide practitioners. For instance, we introduced a first attempt to explore the rainfall effect in the form of a variable interaction term (see Figure 3). This allowed us to dive into how the combination of yearly rainfall parameters influences the likelihood of landslide occurrences in space and time. Currently, the use of variable interaction terms in the landslide literature is mostly confined to cases where one of the two

covariates is continuous and the second one is categorical. For instance, Brenning et al. (2015) used this idea to investigate the effect of road distances per lithological class in Ecuador. The only examples where a two-variable interaction has been previously used to explore precipitation effects can be found in Goetz et al. (2015), where the authors explore how precipitation intensities contribute to landslide occurrence probabilities at varying levels of forest cover. The same idea has been recently featured in Johnston et al. (2021) by allowing precipitation to interact with three different land use types. Here, we present an alternative where two aspects of the same meteorological process can interact and be brought into the model as a unique effect. This could be interesting beyond the context of landslide susceptibility. Specifically, we envision this idea as a useful tool in landslide early warning systems, where the modeling target is usually determined by intensity-duration relationships (e.g., Rossi et al., 2012).

Another nested experiment corresponds to the use of an RCV routine where a larger proportion of the space-time data are progressively taken away from the calibration phase and merged into the prediction subset. The common practice mostly corresponds to a single fixed data split (e.g., Rossi et al., 2010) and the model sensitivity to the proportion of data allocated to the fitting and testing phases is hardly acknowledged. Here, we touch on this subject by exploring the results produced by 100 RCVs obtained from five separate schemes, moving from a 90/10 to a 50/50 split. Interestingly, the last data split takes away a significant amount of data without being followed by a proportional loss in predictive performance. This attests to a robust model, whose stability is reached even when potential space-time autocorrelation effects are necessarily broken at this level of data-removal. Another strength we recognize is using a space-time model for scenario-making purposes. In landslide susceptibility studies, this has been explored in a limited number of contributions. For instance, Steger et al. (2023) take a similar stance for predicting landslides on a daily time step. Recently, Knevels et al. (2023) make use of an analogous simulations framework by fitting a binomial GAM and generating landslide scenarios for a complex combination of future environmental (climate, and land use projections) conditions in Austria. Here, we take a simpler approach by simulating only the rainfall projections. However, we extend the research to combine exposure information to generate risk scenarios. This is also an area where the landslide literature is explored to a lesser extent as compared to the amount of pure landslide susceptibility studies. Valuable contributions on landslide risk do exist, and a number of milestones can be found in the work laid out by (Guzzetti, 2000; Corominas et al., 2014). However, they are mostly confined to current risk assessments and rarely feature elements of predictive modeling (Malek et al., 2015; Rossi et al., 2019).

5.2 Opposing arguments

A number of limitations affect the analyses we present here. The most evident is in the way we

generate landslide occurrence probability projections. In fact, we simulate by changing only the rainfall patterns. This implies that all the other predictors are kept constant even in future years. This assumption may be reasonable for covariates that typically exhibit a low rate of temporal change such as the DEM derivatives. However, it may be considered a limitation in the case of the NDVI. However, we did not have access to vegetation density projections. This being said, the rate at which the NDVI changed through time across the study area appears to be minor and therefore, we also assume this to produce a negligible bias. Also, what we are proposing here is an approach to model space-time risk, and future work can be further extended to account for the issues we noted during the present experiment. Another potential source of bias may reside in the difference in spatial resolution between different rainfall products. In fact, if the native rainfall information is expressed daily both at the level of the local rain gauge network and in the climate projections, the same cannot be said in the spatial dimension. The rain gauges network in the northeast sector of Chongqing is particularly dense, with the maximum distance between two neighboring stations being approximately 20km whereas the average distance is 7.2 km. However, the raw rainfall projections have a native resolution of approximately 26 km $\times$ 26km. This is to stress that the capacity at which the precipitation signal is represented in the fitted model (although interpolated) is higher than the rainfall counterpart used for the simulation phase (although downscaled). This may potentially represent an issue in the uncertainty propagation from one modeling step to the next and future research direction may involve an intermediate phase where a bias-reduction step will be required to minimize the difference between observed and predicted rainfall.

Moving toward the risk component of the present research, some limitations also apply to the exposure data. In fact, the raw projections are based on a five-year time step. As a result, our yearly susceptibility scenarios vary at a higher frequency compared to the built-up area and population layers. This being said, it is reasonable for this to be the case because landslide-prone conditions may be indeed quite different from one year to the next, whereas the urban fabric and its inhabitants vary at a lower rate. Nevertheless, an ideal situation would correspond to a one-to-one correspondence, and future efforts may be dedicated to producing in-house exposure projections at a higher temporal resolution.

6 Concluding remarks

This contribution presents an analytical protocol where the landslide risk projections are obtained as a combination of simulated susceptibility estimates and two separate exposure parameters (built-up areas and local population). This experimental design may constitute the foundation on urban planners to base their decisions on because we integrate two fundamental aspects in risk assessments: spatial and temporal probabilities together with exposure data. We stress that the model we present is just a prototype

and further improvements are required to fulfill the risk definition. In fact, to complete the landslide hazard assessment, the spatiotemporal probabilities need to be associated with the expected landslide intensities. To accommodate for this, we currently exploring a class of models where landslide areas can be jointly predicted in space and time together with the susceptibility. Another requirement that is prohibitive to get access to for such a large area corresponds to vulnerability curves, at least for the major infrastructure and building of interest. Even in this case, we are collaborating with local institutes to generate vulnerability data and their potential variations in space and time.

Overall, we believe this type of modeling framework holds great potential in the framework of landslide prediction at large. In fact, its structure can be flexibly adapted to local spatial and daily temporal domains offering solutions in line with early warning systems. And, if adapted to regional spatial and yearly temporal domains, it can offer solutions in line with scenario projections. The addition of the exposure components ensures the extension of the probabilistic results towards an integrated risk modeling approach, whose full potential may be unlocked once urban-finance data will be collected and analyzed for loss quantification.

Author contributions statement

Luigi Lombardo has devised the experiment, written the manuscript, and produced the scientific illustrations. **Tengfei Wang** has pre-processed the data, run all the analyses, produced the scientific illustrations, and written the manuscript. **Ashok Dahal** has helped with computing the rainfall projections and writing the manuscript and figures. **Zhice Fang** has helped with the model implementation. **Cees van Westen** has taken part in different stages of the experiment, mainly contributing to the discussion and the critical revision of the research idea. **Kunlong Yin** is the data provider and formal doctoral supervisor of **Tengfei Wang**.

Acknowledgement

References

Abella, E. C. and Van Westen, C. (2007) Generation of a landslide risk index map for Cuba using spatial multi-criteria evaluation. Landslides **4**(4), 311–325.

Agostinelli, C., 2002. Robust stepwise regression. *Journal of Applied Statistics*, *29*(6), pp.825-840.

579   Ahmed, B. (2021) The root causes of landslide vulnerability in Bangladesh. Landslides **18**(5), 1707–1720.

580   Alvioli, M., Marchesini, I., Reichenbach, P., Rossi, M., Ardizzone, F., Fiorucci, F and Guzzetti,
581   F. (2016) Automatic delineation of geomorphological slope units with r. slopeunits v1.0 and their
582   optimization for landslide susceptibility modeling. Geoscientific Model Development **9**(11), 3975–3991.

583   Amato, G., Eisank, C., Castro-Camilo, D. and Lombardo, L., 2019. Accounting for covariate
584   distributions in slope-unit-based landslide susceptibility models. A case study in the alpine
585   environment. Engineering geology, 260, p.105237.

586   Babak, O., Deutsch, C.V., 2009. Statistical approach to inverse distance interpolation. Stochastic
587   Environmental Research and Risk Assessment 23, 543–553.

588   Beck, N., Katz, J.N., Tucker, R., 1998. Taking time seriously: Time-series-cross-section analysis with a
589   binary dependent variable. American Journal of Political Science 42, 1260–1288.

590   Brenning, A. (2012) Spatial cross-validation and bootstrap for the assessment of prediction rules in remote
591   sensing: The r package sperrorest. In 2012 IEEE international geoscience and remote sensing symposium,
592   pp. 5372–5375.

593   Brenning, A., 2008. Statistical geocomputing combining R and SAGA: The example of landslide
594   susceptibility analysis with generalized additive models. Hamburger Beiträge zur Physischen
595   Geographie und Landschaftsökologie 19, 410.

596   Brenning, A., Schwinn, M., Ruiz-Páez, A. and Muenchow, J. (2015) Landslide susceptibility near highways
597   is increased by 1 order of magnitude in the Andes of southern Ecuador, Loja province. Natural
598   Hazards and Earth System Sciences **15**(1), 45–57.

599   Budimir, M., Atkinson, P. and Lewis, H. (2015) A systematic review of landslide probability mapping
600   using logistic regression. Landslides **12**(3), 419–436.

601   Calcaterra, D., Di Martire, D., Palma, B. and Parise, M. (2010) Assessing landslide risk through unique
602   condition units.

603   Carrara, A. (1988) Drainage and divide networks derived from high-fidelity digital terrain models. In
604   Quantitative analysis of mineral and energy resources, pp. 581–597. Springer.

605   Carrara, A., Cardinali, M., Detti, R., Guzzetti, F., Pasqui, V. and Reichenbach, P. (1991) Gis techniques
606   and statistical models in evaluating landslide hazard. Earth surface processes and landforms 16(5),
607   427–445.

608   Chen, S., Yan, Y., Liu, G., Fang, D., Wu, Z., He, J. and Tang, J. (2019) Spatiotemporal characteristics
609   of precipitation diurnal variations in Chongqing with complex terrain. Theoretical and Applied
610   Climatology **137**, 1217–1231.

Conoscenti, C., Rotigliano, E., Cama, M., Caraballo-Arias, N. A., Lombardo, L. and Agnesi,V. (2016) Exploring the effect of absence selection on landslide susceptibility models: A case study in Sicily, Italy. Geomorphology **261**, 222–235.

Corominas, J., van Westen, C., Frattini, P., Cascini, L., Malet, J.-P., Fotopoulou, S., Catani, F., Van Den Eeckhaut, M., Mavrouli, O., Agliardi, F. et al. (2014) Recommendations for the quantitative analysis of landslide risk. Bulletin of engineering geology and the environment **73**, 209–263.

Cressie, N. (1988) Spatial prediction and ordinary kriging. Mathematical geology 20, 405–421.

Dai, F., Lee, C. F. and Ngai, Y. Y. (2002) Landslide risk assessment and management: an overview. Engineering geology **64**(1), 65–87.

Emberson, R., Kirschbaum, D. and Stanley, T. (2020) New global characterisation of landslide exposure. Natural Hazards and Earth System Sciences **20**(12), 3413–3424.

Fang, Z., Wang, Y., Peng, L. and Hong, H. (2020) Integration of convolutional neural network and conventional machine learning classifiers for landslide susceptibility mapping. Computers & Geosciences **139**, 104470.

Fluss, R., Faraggi, D., Reiser, B., 2005. Estimation of the Youden Index and its associated cutoff point. Biometrical Journal: Journal of Mathematical Methods in Biosciences 47, 458–472.

Galli, M. and Guzzetti, F. (2007) Landslide vulnerability criteria: a case study from Umbria, Central Italy. Environmental management **40**(4), 649–665.

Glade, T., Anderson, M. G. and Crozier, M. J. (2005) Landslide hazard and risk. Volume **807**. Wiley Online Library.

Goetz, J., Guthrie, R. and Brenning, A. (2015) Forest harvesting is associated with increased landslide activity during an extreme rainstorm on Vancouver Island, Canada. Natural Hazards and Earth System Sciences **15**(6), 1311–1330.

Gong, P., Chen, B., Li, X., Liu, H., Wang, J., Bai, Y., Chen, J., Chen, X., Fang, L., Feng, S. et al. (2020) Mapping essential urban land use categories in China (EULUC-China): Preliminary results for 2018. Science Bulletin **65**(3), 182–187.

Guzzetti, F. (2000) Landslide fatalities and the evaluation of landslide risk in Italy. Engineering Geology 58(2), 89–107.

Hajian-Tilaki, K., 2013. Receiver operating characteristic (ROC) curve analysis for medical diagnostic test evaluation. Caspian journal of internal medicine 4, 627.

Hastie, T., Tibshirani, R., 1987. Generalized additive models: some applications. Journal of the American Statistical Association 82, 371–386.

643 Hastie, T.J., 2017. Generalized additive models, in: Statistical Models in S. Routledge, pp. 249–307.

644 Hosmer, D. W. and Lemeshow, S. (2000) Applied Logistic Regression. Second edition. New York:
645   Wiley.

646 Ihaka, R., Gentleman, R., 1996. R: a language for data analysis and graphics. Journal of computational
647   and graphical statistics 5, 299–314.

648 Jasiewicz, J. and Stepinski, T. F. (2013) Geomorphons—a pattern recognition approach to classification
649   and mapping of landforms. Geomorphology **182**, 147–156.

650 Jenson, S. K. and Domingue, J. O. (1988) Extracting topographic structure from digital elevation data
651   for geographic information system analysis. Photogrammetric engineering and remote sensing
652   **54**(11), 1593–1600.

653 Johnston, E. C., Davenport, F. V., Wang, L., Caers, J. K., Muthukrishnan, S., Burke, M. and Diffenbaugh,
654   N. S. (2021) Quantifying the effect of precipitation on landslide hazard in urbanized and non-
655   urbanized areas. Geophysical Research Letters **48**(16), e2021GL094038.

656 Kaynia, A., Papathoma-K¨ohle, M., Neuh¨auser, B., Ratzinger, K., Wenzel, H. and Medina-Cetina, Z.
657   (2008) Probabilistic assessment of vulnerability to landslide: application to the village of
658   Lichtenstein, Baden-Wu¨rttemberg, Germany. Engineering Geology **101**(1-2), 33–48.

659 Knevels, R., Petschko, H., Proske, H., Leopold, P., Mishra, A. N., Maraun, D. and Brenning, A. (2023)
660   Assessing uncertainties in landslide susceptibility predictions in a changing environment (Styrian Basin,
661   Austria). Natural Hazards and Earth System Sciences **23**(1), 205–229.

662 Lateltin, O., Haemmig, C., Raetzo, H. and Bonnard, C. (2005) Landslide risk management in
663   Switzerland. Landslides **2**(4), 313–320.

664 Lepetit, Q., Vigui´e, V. and Liotta, C. (2023) A gridded dataset on densities, real estate prices, transport,
665   and land use inside 192 worldwide urban areas. Data in Brief **47**, 108962.

666 Li, B., Gao, Y., Yin, Y., Wan, J., He, K., Wu, W. and Zhang, H. (2022) Rainstorm-induced large-scale
667   landslides in Northeastern Chongqing, China, August 31 to September 2, 2014. Bulletin of
668   Engineering Geology and the Environment **81**(7), 271.

669 Li, Y., Liu, C. and Yuan, X. (2009) Spatiotemporal features of soil and water loss in Three Gorges
670   Reservoir Area of Chongqing. Journal of Geographical Sciences **19**(1), 81–94.

671 Lima, P., Steger, S. and Glade, T. (2021) Counteracting flawed landslide data in statistically based
672   landslide susceptibility modelling for very large areas: a national-scale assessment for Austria.
673   Landslides **18**(11), 3531–3546.

674 Lima, P., Steger, S., Glade, T. and Murillo-Garc´ıa, F. G. (2022) Literature review and bibliometric

analysis on data-driven assessment of landslide susceptibility. Journal of Mountain Science **19**(6), 1670–1698.

Lombardo, L., Bakka, H., Tanyas, H., van Westen, C., Mai, P. M. and Huser, R. (2019) Geostatistical modeling to capture seismic-shaking patterns from earthquake-induced landslides. Journal of Geophysical Research: Earth Surface **124**(7), 1958–1980.

Lombardo, L., Opitz, T., Ardizzone, F., Guzzetti, F. and Huser, R. (2020) Space-time landslide predictive modelling. Earth-Science Reviews p. 103318.

Lombardo, L., Saia, S., Schillaci, C., Mai, P. M. and Huser, R. (2018) Modeling soil organic carbon with Quantile Regression: Dissecting predictors' effects on carbon stocks. Geoderma **318**, 148–159.

Lombardo, L. and Tanyas, H. (2020) Chrono-validation of near-real-time landslide susceptibility models via plug-in statistical simulations. Engineering Geology **278**, 105818.

Luo, H., Zhang, L., Zhang, L., He, J. and Yin, K. (2023) Vulnerability of buildings to landslides: The state of the art and future needs. Earth-Science Reviews p. 104329.

Luo, L., Lombardo, L., van Westen, C., Pei, X. and Huang, R. (2021) From scenario-based seismic hazard to scenario-based landslide hazard: rewinding to the past via statistical simulations. Stochastic environmental research and risk assessment pp. 1–22.

Malek, Ž., Boerboom, L. and Glade, T. (2015) Future forest cover change scenarios with implications for landslide risk: an example from Buzau Subcarpathians, Romania. Environmental Management **56**, 1228–1243.

McDonald, G.C., 2009. Ridge regression. Wiley Interdisciplinary Reviews: Computational Statistics, 1(1), pp.93-100.

Meijerink, A. (1988) Data acquisition and data capture through terrain mapping unit. ITC Jour. **1**, 23–24.

Mondini, A. C., Guzzetti, F. and Melillo, M. (2023) Deep learning forecast of rainfall-induced shallow landslides. Nature Communications **14**(1), 2466.

Nocentini, N., Rosi, A., Segoni, S., Fanti, R., et al. (2023) Towards landslide space-time forecasting through machine learning: the influence of rainfall parameters and model setting. Frontiers in Earth Science **11**, 1–20.

North, M. A. (2009) A method for implementing a statistically significant number of data classes in the Jenks algorithm. In 2009 Sixth International Conference on Fuzzy Systems and Knowledge Discovery, volume **1**, pp. 35–38.

Opitz, T., Bakka, H., Huser, R. and Lombardo, L. (2022) High-resolution Bayesian mapping of landslide

hazard with unobserved trigger event. The Annals of Applied Statistics **16**(3), 1653–1675.

Ozturk, U., Pittore, M., Behling, R., Roessner, S., Andreani, L. and Korup, O. (2021) How robust are landslide susceptibility estimates? Landslides **18**, 681–695.

Papathoma-K¨ohle, M., Zischg, A., Fuchs, S., Glade, T. and Keiler, M. (2015) Loss estimation for landslides in mountain areas–An integrated toolbox for vulnerability assessment and damage documentation. Environmental Modelling & Software **63**, 156–169.

Pascale, S., Sdao, F. and Sole, A. (2010) A model for assessing the systemic vulnerability in landslide prone areas. Natural Hazards and Earth System Sciences **10**(7), 1575–1590.

Peduto, D., Ferlisi, S., Nicodemo, G., Reale, D., Pisciotta, G. and Gullà, G. (2017) Empirical fragility and vulnerability curves for buildings exposed to slow-moving landslides at medium and large scales. Landslides **14**, 1993–2007.

Pellicani, R., Van Westen, C. J. and Spilotro, G. (2014) Assessing landslide exposure in areas with limited landslide information. Landslides **11**, 463–480.

Petley, D. (2012) Global patterns of loss of life from landslides. Geology **40**(10), 927–930.

Petschko, H., Brenning, A., Bell, R., Goetz, J. and Glade, T. (2014) Assessing the quality of landslide susceptibility maps—case study Lower Austria. Natural Hazards and Earth System Sciences **14**(1), 95–118.

Quan Luna, B., Blahut, J., Van Westen, C., Sterlacchini, S., van Asch, T. W. and Akbas, S. (2011) The application of numerical debris flow modelling for the generation of physical vulnerability curves. Natural hazards and earth system sciences **11**(7), 2047–2060.

Reichenbach, P., Rossi, M., Malamud, B. D., Mihir, M. and Guzzetti, F. (2018) A review of statistically-based landslide susceptibility models. Earth-Science Reviews **180**, 60–91.

Remondo, J., Bonachea, J. and Cendrero, A. (2008) Quantitative landslide risk assessment and mapping on the basis of recent occurrences. Geomorphology **94**(3-4), 496–507.

Roberts, D. R., Bahn, V., Ciuti, S., Boyce, M. S., Elith, J., Guillera-Arroita, G., Hauenstein, S., Lahoz-Monfort, J. J., Schr¨oder, B., Thuiller, W., et al. (2017) Cross-validation strategies for data with temporal, spatial, hierarchical, or phylogenetic structure. Ecography **40**(8), 913–929.

Rossi, M., Guzzetti, F., Reichenbach, P., Mondini, A. C. and Peruccacci, S. (2010) Optimal landslide susceptibility zonation based on multiple forecasts. Geomorphology **114**(3), 129–142.

Rossi, M., Guzzetti, F., Salvati, P., Donnini, M., Napolitano, E. and Bianchi, C. (2019) A predictive model of societal landslide risk in Italy. Earth-Science Reviews **196**, 102849.

Rossi, M., Peruccacci, S., Brunetti, M., Marchesini, I., Luciani, S., Ardizzone, F., Balducci, V., Bianchi,

C., Cardinali, M., Fiorucci, F., et al. (2012) SANF: National warning system for rainfall-induced landslides in Italy. <u>Landslides and engineered slopes: protecting society through improved understanding</u> **2**, 1895–1899.

Sakamoto, Y., Ishiguro, M., Kitagawa, G., 1986. Akaike information criterion statistics. Dordrecht, The Netherlands: D. Reidel 81, 26853.

Samia, J., Temme, A. J., Bregt, A., Wallinga, J., Guzzetti, F., Ardizzone, F. and Rossi, M. (2017) Do Landslides Follow Landslides? Insights in Path Dependency from a Multi-Temporal Landslide Inventory. <u>Landslides</u> **14**, 547–558.

Schlögel, R., Marchesini, I., Alvioli, M., Reichenbach, P., Rossi, M. and Malet, J.-P. (2018) Optimizing landslide susceptibility zonation: Effects of DEM spatial resolution and slope unit delineation on logistic regression models. <u>Geomorphology</u> **301**, 10–20.

Segoni, S., Piciullo, L. and Gariano, S. L. (2018) A review of the recent literature on rainfall thresholds for landslide occurrence. <u>Landslides</u> **15**(8), 1483–1501.

Seijmonsbergen, A. <u>et al.</u> (2013) The modern geomorphological map. In: <u>Methods in geomorphology</u>, Elsevier, Amsterdam, pp.35-52.

Steger, S., Brenning, A., Bell, R. and Glade, T. (2016) The propagation of inventory-based positional errors into statistical landslide susceptibility models. <u>Natural Hazards and Earth</u> <u>System Sciences</u> **16**(12), 2729–2745.

Steger, S., Moreno, M., Crespi, A., Zellner, P. J., Gariano, S. L., Brunetti, M. T., Melillo, M., Peruccacci, S., Marra, F., Kohrs, R. <u>et al.</u> (2022) Deciphering seasonal effects of triggering and preparatory precipitation for improved shallow landslide prediction using generalized additive mixed models. <u>Natural Hazards and Earth System Sciences Discussions</u> pp. 1–38.

Steger, S., Moreno, M., Crespi, A., Zellner, P. J., Gariano, S. L., Brunetti, M. T., Melillo, M., Peruccacci, S., Marra, F., Kohrs, R. <u>et al.</u> (2023) Deciphering seasonal effects of triggering and preparatory precipitation for improved shallow landslide prediction using generalized additive mixed models. <u>Natural Hazards and Earth System Sciences</u> **23**(4), 1483–1506.

Taylor, K. E., Stouffer, R. J. and Meehl, G. A. (2012) An overview of CMIP5 and the experiment design. <u>Bulletin of the American Meteorological Society</u> **93**(4), 485–498.

Thrasher, B., Maurer, E. P., McKellar, C., and Duffy, P. B. (2012) Technical Note: Bias correcting climate model simulated daily temperature extremes with quantile mapping. <u>Hydrology and Earth System Sciences</u> **16**(9), 3309–3314.

Titti, G., van Westen, C., Borgatti, L., Pasuto, A. and Lombardo, L. (2021) When enough is really

enough? on the minimum number of landslides to build reliable susceptibility models. Geosciences **11**(11), 469.

Tyagi, A., Tiwari, R. K. and James, N. (2022) A review on spatial, temporal and magnitude prediction of landslide hazard. Journal of Asian Earth Sciences: X p. 100099.

Uzielli, M., Catani, F., Tofani, V. and Casagli, N. (2015) Risk analysis for the Ancona landslide—II: estimation of risk to buildings. Landslides **12**, 83–100.

Van Den Eeckhaut, M., Reichenbach, P., Guzzetti, F., Rossi, M. and Poesen, J. (2009) Combined landslide inventory and susceptibility assessment based on different mapping units: an example from the Flemish Ardennes, Belgium. Natural Hazards and Earth System Sciences **9**(2), 507–521.

Van Westen, C., Van Asch, T. W. and Soeters, R. (2006) Landslide hazard and risk zonation—why is it still so difficult? Bulletin of Engineering Geology and the Environment **65**(2), 167–184.

Wadoux, A. M.-C., Heuvelink, G. B., De Bruin, S. and Brus, D. J. (2021) Spatial cross-validation is not the right way to evaluate map accuracy. Ecological Modelling **457**, 109692.

Wang, L., Yin, Y., Zhang, Z., Huang, B., Wei, Y., Zhao, P., and Hu, M. (2019) Stability analysis of the Xinlu Village landslide (Chongqing, China) and the influence of rainfall. Landslides **16**, 1993–2004.

Wang, N., Cheng, W., Marconcini, M., Bachofer, F., Liu, C., Xiong, J. and Lombardo, L. (2022a) Space-time susceptibility modeling of hydro-morphological processes at the Chinese national scale. Engineering geology **301**, 106586.

Wang, Z., Goetz, J. and Brenning, A. (2022b) Transfer learning for landslide susceptibility modeling using domain adaptation and case-based reasoning. Geoscientific Model Development **15**(23), 8765–8784.

Wood, S. and Wood, M.S., 2015. Package 'mgcv'. R package version, 1(29), p.729.

Yilmaz, I. (2010) The effect of the sampling strategies on the landslide susceptibility mapping by conditional probability and artificial neural networks. Environmental Earth Sciences **60**, 505–519.

Zhang, W., He, Y., Wang, L., Liu, S. and Meng, X. (2023) Landslide Susceptibility mapping using random forest and extreme gradient boosting: A case study of Fengjie, Chongqing. Geological Journal.

Zhao, L., Zuo, S., Deng, D., Han, Z. and Zhao, B. (2018) Development mechanism for the landslide at Xinlu Village, Chongqing, China. Landslides **15**, 2075–2081.